3D Beam-Steering MIMO Antenna for On-Body IoT Applications

Abel Zandamela, *Graduate Student Member, IEEE,* Nicola Marchetti, *Senior Member, IEEE,*
Max, J. Ammann, *Fellow, IEEE,* and Adam Narbudowicz, *Senior Member, IEEE*

Abstract—In this article, a compact 3D beam-steering MIMO antenna operating at 5.75 GHz is proposed for on-body Internet of Things (IoT) applications. The planar antenna comprises a central patch and two concentric annular rings. The theory of spherical modes is used to discuss the beam-steering concept, where the free space measured beam-scanning covers the entire xy-plane, while a $44°$ range is realized in xz and yz-planes. The on-body performance is tested using a multi-layer phantom, and the measured peak realized gain is 6.41 dBi. The antenna is characterized by compact size (0.77λ), low profile (0.03λ), specific absorption rate below the established limits, good efficiency and 3D beam-steering characteristics while operating in an on-body setup. Therefore, the proposed solution can enable advanced wireless applications like localization and physical layer security in emerging size-constrained on-body IoT devices.

Index Terms—On-body antennas, MIMO antennas, beam-steering antennas, planar antennas, spherical modes.

I. INTRODUCTION

BEAM-STEERING antennas are an actively researched topic due to their ability to alter the antenna-generated radiation pattern. This feature enhances numerous aspects of modern wireless communication systems, e.g. spatial coverage, spectral efficiency, and interference mitigation [1]–[3].

Recently, different methods have been proposed to realize compact beam-steering antennas, e.g. in the azimuth plane [4]–[9], or in the elevation plane [10]–[14]. However, because of size and profile, integrating these solutions into on-body IoT systems is still a challenging problem. Also, only a few works have investigated compact beam-steering antennas covering both the azimuth and elevation planes. In [15], [16], stacked patches are used for full-scan in the azimuth plane and a $120°$ coverage in the elevation plane. In [17], a highly pattern-reconfigurable Alford loop antenna is proposed for 3D full-space scanning. While these antennas offer a wide-scanning range, the structures are of relatively large diameter [17] ($> 1.39\lambda$, where λ is the wavelength at the center frequency);

A. Zandamela and N. Marchetti are with CONNECT Centre, Trinity College Dublin, The University of Dublin, D02PN40, Ireland (e-mail: zandamea@tcd.ie; nicola.marchetti@tcd.ie).

Max J. Ammann is with the Antenna and High Frequency Research Centre, School of Electrical and Electronic Engineering, Technological University Dublin, D07ADY7, Dublin, Ireland (e-mail: max.ammann@tudublin.ie).

A. Narbudowicz is with CONNECT Centre, Trinity College Dublin, The University of Dublin, D02PN40, Ireland, and also with the Department of Telecommunications and Teleinformatics, Wroclaw University of Science and Technology, Wroclaw 50-370, Poland (e-mail:narbudoa@tcd.ie).

or else, the designs are bulky and not planar, with profile $> 0.2\lambda$, which is still relatively high for on-body IoT devices [15], [16].

On-body beam-steering antennas have been proposed in [18]–[29]. Elevation plane beam-steering is discussed in [18]. A dual-mode pattern synthesis (omnidirectional and broadside) is achieved in [19]–[21]. In [22], the theory of characteristic modes is used to design a dual-port metal-frame smart watch antenna capable of changing between a bidirectional and an omnidirectional pattern in the xz and yz-planes. Lastly, a dual-mode pattern synthesis is obtained in [28] (using tunable ring slots and p-i-n diodes) and in [29] (using rectangular patches loaded with rectangular slots and p-i-n diodes). However, the beam-steering performance of these works is still limited to only yz-plane [18], dual-mode patterns [19]–[21], [28], [29], or bidirectional and omnidirectional patterns in xz and yz-planes [22]. Recently, in [30], we exploited the theory of spherical modes to design a stacked-patch beam-steering antenna for directional modulation applications. Although the diameter is around $\lambda/2$, it only allows for beam-steering in the xy-plane, is not planar, and has a 0.063λ profile, which limits its use for on-body IoT scenarios, e.g., integration with a smart watch.

In this work, we propose for the first time a compact and planar 3D beam-steering on-body antenna. The theory of spherical modes [31] is used to describe the antenna beam-steering in the xy-plane, and the beam-scanning is extended to cover the xz and yz-planes through the excitation of broadside modes. A measured $360°$ xy-plane scan is realized for both free space and on-body operation. A $44°$ coverage is demonstrated in free space for xz and yz-planes, reducing to around $32°$ for the on-body case. The simulated total efficiency is $\geq 73\%$, and the peak gain is 8.61 dBi in free space, decreasing to respectively 58% and 7.8 dBi with the phantom. This increased antenna gain allows improved signal strength, reduces battery use, and enables angle of arrival localization, to name just a few benefits. The remainder of this article is organized as follows. Section II discusses the beam-steering principle and antenna design. Section III presents the free space performance, and the on-body performance is discussed in Section IV. Finally, conclusions are presented in Section V.

II. BEAM-STEERING PRINCIPLE AND ANTENNA DESIGN

A. Spherical Modes Analysis

The electric field $\vec{E}(r,\theta,\phi)$ can be represented as a weighted sum of spherical modes functions $\vec{F}_{smn}^{(c)}(r,\theta,\phi)$, and assuming the e^{-iwt} time dependency this is expressed as [32]

$$\vec{E}(r,\theta,\phi) = \frac{k}{\sqrt{\eta}} \sum_{csmn} Q_{smn}^{(c)} \vec{F}_{smn}^{(c)}(r,\theta,\phi) \quad (1)$$

where $k = 2\pi/\lambda$ is the wavenumber, λ is the wavelength, η is the specific impedance of the medium, and $Q_{smn}^{(c)}$ are the spherical modes coefficients. The index s is related to polarization (used to distinguish between two functions); for transverse magnetic (TM) waves, $s = 1$ corresponds to the magnetic fields, and $s = 2$ represents the electric fields, while this is reversed for the transverse electric (TE) waves. The index $n = 1, 2, \cdots, N$ denotes the order of the spherical mode, and m ($|m| \leq n$) denotes the azimuthal phase variations. The upper index c specifies a radial function, where $c = 1, 2$ are standing waves, $c = 3$ and $c = 4$ represent the outward and inward traveling waves, respectively. The spherical modes' vector fields $\vec{F}_{smn}^{(c)}(r,\theta,\phi)$ are power-normalized dimensionless solutions of the vector wave equation and are defined in [32] and [33]. A general outgoing wave field can then be written as $\vec{E}(r,\theta,\phi) = \frac{k}{\sqrt{\eta}} \sum_{smn} Q_{smn}^{(3)} \vec{F}_{smn}^{(3)}(r,\theta,\phi)$. At a large distance ($kr \to \infty$), the far-field can be described solely in terms of the angular variables (θ,ϕ) as

$$\vec{K}_{smn}(\theta,\phi) = \lim_{kr\to\infty}\left[\sqrt{4\pi}\frac{kr}{e^{ikr}}\vec{F}_{smn}^{(3)}(r,\theta,\phi)\right] \quad (2)$$

The far-field functions can then be defined explicitly as [32]

$$\vec{K}_{1mn}(\theta,\phi) = \sqrt{\frac{2}{n(n+1)}}\left(-\frac{m}{|m|}\right)^m e^{im\phi}(-i)^{n+1}$$
$$\left\{\frac{im\bar{P}_n^{|m|}(\cos\theta)}{\sin\theta}\vec{e}_\theta - \frac{d\bar{P}_n^{|m|}(\cos\theta)}{d\theta}\vec{e}_\phi\right\} \quad (3)$$

$$\vec{K}_{2mn}(\theta,\phi) = \sqrt{\frac{2}{n(n+1)}}\left(-\frac{m}{|m|}\right)^m e^{im\phi}(-i)^{n}$$
$$\left\{\frac{d\bar{P}_n^{|m|}(\cos\theta)}{d\theta}\vec{e}_\theta + \frac{im\bar{P}_n^{|m|}(\cos\theta)}{\sin\theta}\vec{e}_\phi\right\} \quad (4)$$

Note that the radius component of $\vec{F}_{smn}^{(3)}(r,\theta,\phi)$ now disappears, as it is intrinsic to the far-field region. In terms of $\vec{K}_{smn}(\theta,\phi)$ the $\vec{E}$-field at a large distance is then given by

$$\vec{E}(r,\theta,\phi) \to \frac{k}{\sqrt{\eta}}\frac{1}{\sqrt{4\pi}}\frac{e^{ikr}}{kr}\sum_{smn}Q_{smn}^{(3)}\vec{K}_{smn}(\theta,\phi) \quad (5)$$

B. Beam-Steering Principle

Let us assume that an antenna can be fully enclosed by a sphere of smallest radius r_0 (see Fig. 1), and radiates omnidirectional spherical modes of type $s = 1$ so that indexes n and m of each mode (for $n \geq 2$) are related as follows

$$m = \pm n \quad (6)$$

The modes satisfying the above condition can be expressed as $\vec{K}_{1,\pm N,N}$. To realize beam-steering in the whole azimuth plane, a MIMO system is designed to excite all omnidirectional spherical modes of order $N, N-1, \cdots 1$ that can be supported within the enclosing sphere of radius $\leq r_0$. Except for the fundamental mode ($n = 1$ with $m = 0$, i.e., $\vec{K}_{smn} = \vec{K}_{1,0,1}$), which has a constant phase across the entire xy-plane, the remaining modes have their phase changing in two opposite directions, $\pm N, \pm(N-1), \cdots$; where the "$+$"
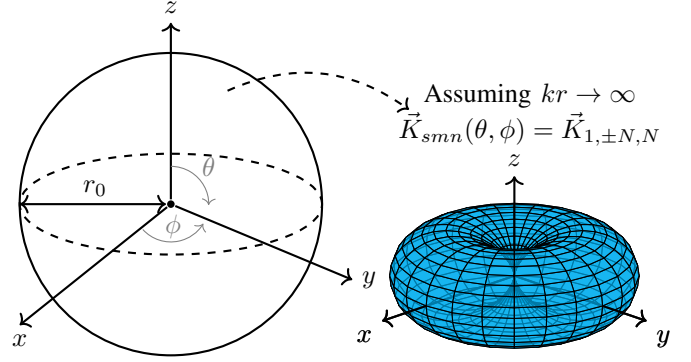

Fig. 1. Visualization of the smallest sphere that fully encloses an antenna exciting omnidirectional spherical modes (amplitudes shown on the right).

sign indicates clockwise rotation, and the "$-$" sign denotes counter-clockwise rotation. The beam-steering towards ϕ_a direction is then realized using

$$D(\theta,\phi_a) = w_1\vec{K}_{1,0,1}(\theta,\phi_a) + \sum_{n=2}^{N}w_n\vec{K}_{1,\pm n,n}(\theta,\phi_a) \quad (7)$$

where $D(\theta,\phi_a)$ is the maximum directivity in a given θ-cut, $w_n = |A_n|e^{j\Delta\beta_n}$ term is a weighting factor applied at the port exciting the respective omnidirectional spherical mode, $|A_n|$ and $\Delta\beta_n$ are the magnitude and phase shift, respectively.

The fundamental mode ($\vec{K}_{1,0,1}$) has a constant phase across the entire xy-plane, hence it is used as the reference mode when computing the required phase shift

$$\Delta\beta_n = \beta_{\vec{K}_{1,0,1}}(\phi_a) - \beta_{\vec{K}_{1,m,n}}(\phi_a) \quad (8)$$

where $\beta_{\vec{K}_{1,0,1}}(\phi_a)$ and $\beta_{\vec{K}_{1,m,n}}(\phi_a)$ is the phase value of $\vec{K}_{1,0,1}$ and the phase-varying mode, respectively.

C. Spherical Modes Based Planar Beam-Steering Antennas

To implement the proposed principle in on-body devices, a centrally located patch and concentric annular rings are used to design a planar structure. The $\vec{K}_{1,0,1}$ mode is excited using a central circular patch, while the phase-varying modes are excited using concentric annular rings. Fig. 2 shows a planar configuration, where each structure excites a total of $l = 1, 2, 3, \cdots$ omnidirectional spherical modes. The structures are supported by a $1.52\,\text{mm}$ thick RO4003C substrate ($\epsilon_r = 3.38$, $\tan\delta = 0.0027$) and operate at the center frequency $f_0 = 5.8\,\text{GHz}$. The metallic radiators and the ground plane are made of a $35\,\mu\text{m}$ thick copper (5.8e7 S/m), and the shorting pins are also made of copper, but with $0.5\,\text{mm}$ diameter.

Radiator A is a center-fed patch (using P1) with $14\,\text{mm}$ diameter. The patch excites the single fundamental spherical mode ($l = 1$). It includes four shorting pins ($n_{pins} = 4$) located at $v_1 = 2.75\,\text{mm}$ away from the center of the patch and rotated by $90°$ with respect to the disk center. Since without the shorting pins ($n_{pins} = 0$), the patch is out of resonance in the investigated frequency range, the integration of the shorting pins allows it to have resonance at the desired f_0 [34], [35]. This is highlighted in Fig. 3a, where n_{pins} varies from 0 to 6. It can be seen that within the investigated
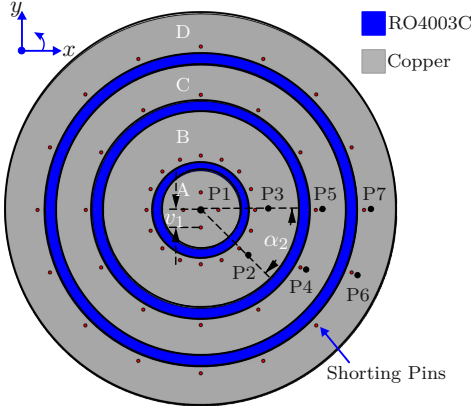
Fig. 2. Proposed antenna: (a) A excites $\vec{K}_{1,0,1}$; B excites $\vec{K}_{1,\pm2,2}$ for bidirectional beam-steering; C excites $\vec{K}_{1,\pm3,3}$ for unidirectional beam-steering; and D excites $\vec{K}_{1,\pm4,4}$ for enhanced directivity.
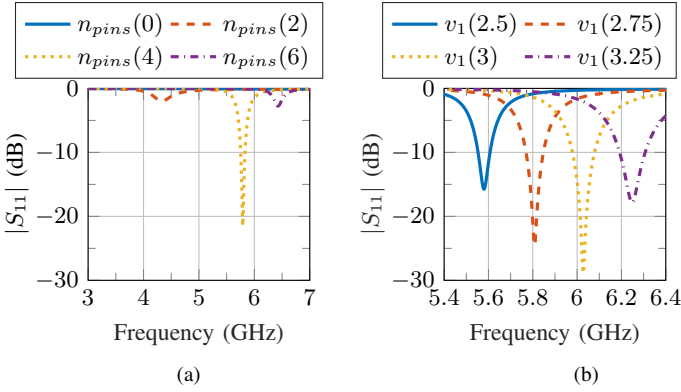

Fig. 3. Parametric results of radiator A: (a) S-parameter results for different numbers of shorting pins; and (b) S-parameter results for different v_1 values.

frequency range, the patch has non-zero resonant frequency for $n_{pins} = 2, 4,$ and, 6, and good matching ($|S_{11}| < -20$ dB) is achieved for $n_{pins} = 4$. It is also important to note that due to the pins' inductance, the frequency shifts upwards for an increased n_{pins} value. Moreover, frequency tuning and matching enhancement can be obtained by adjusting the pins' distance, i.e., v_1 value. This is demonstrated in Fig. 3b, where v_1 is increased from 2.5 mm to 3.25 mm. It can be seen that the frequency increases with v_1, and at $v_1 = 2.75$ mm good matching is observed at the desired $f_0 = 5.8$ GHz.

Ring B in Fig. 2 excites the dual-phase varying modes $\vec{K}_{1,+2,2}$ (P2), and $\vec{K}_{1,-2,2}$ (P3). It has an inner diameter of 15 mm and an outer diameter of 32 mm. The ports P2 and P3 are located 2 mm from the edges of the inner diameter of the ring and are rotated by $\alpha_2 = \pi/4$, computed from

$$\alpha_n = \begin{cases} \frac{\pi}{2}(\frac{1}{n} + u), & n = 2, 4, 6, \cdots; \ u = 0, 1, 2, \cdots \\ \frac{\pi}{6}(\frac{3}{n} + 2u), & n = 3, 5, 7, \cdots; \ u = 0, 1, 2, \cdots \end{cases} \quad (9)$$

where n is the order of the excited mode, and u denotes an integer that can be arbitrarily selected to obtain α_n that satisfies the condition to generate omnidirectional spherical mode of order n. It is introduced here as numerous possible α_n satisfy the required criteria. The ring includes shorting pins for frequency tuning and isolation enhancement, and the pin
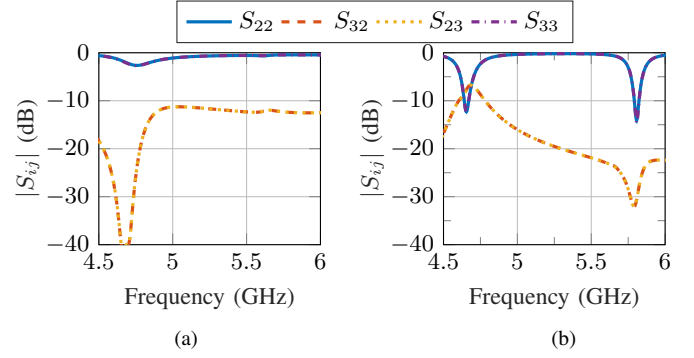

Fig. 4. S-parameters of radiator B, port index $i, j = 2, 3$: (a) results of the annular ring without shorting pins; and (b) results including shorting pins.

numbers need to take into account the ports' position. This is necessary to ensure symmetry between the two excited modes of the same order. For this work, the total number of pins in a given annular ring is calculated using

$$n_{pins} = \frac{2\pi}{\alpha_n}p \quad (10)$$

where α_n is the angle between the two feeds as calculated in (9), whereas $p = 1, 2, 3, \cdots$ is an integer that controls how many pins are located between the two feeds, while taking into account the desired f_0, $|S_{ii}| \leq -10$ dB, and isolation ≥ 10 dB. Please note that (10) also ensures that the pins are located symmetrically with respect to the two ports exciting each ring. Due to the inductance of the pins, an increase in f_0 is observed for larger values of p. For ring B, $p = 2$ is used, and from (10) $n_{pins} = 16$. The pins of this configuration are located 1 mm from the edges of the inner diameter of the ring, and are rotated with respect to the center by $\alpha_{pins} = \pi/8$ obtained using

$$\alpha_{pins} = \frac{\alpha_n}{p} \quad (11)$$

Fig. 4 shows the effect of adding shorting pins into the ring structures, demonstrated for ring B. Fig. 4a shows the case without pins, where it can be seen that while good isolation is obtained at f_0, $|S_{ii}|$ stays above -2.5 dB. In contrast, when $n_{pins} = 16$ are added into the ring (see Fig. 4b), good isolation is obtained with an improvement of the matching ($|S_{ii}| < -14$ dB), while due to the pins inductance, the f_0 is also shifted towards the desired value of 5.8 GHz.

The annular ring C (inner diameter 34 mm and outer diameter 46.8 mm) excites two modes with triple-phase variations ($\vec{K}_{1,\pm3,3}$). The feed ports of these modes (P4 and P5) are located 1.75 mm from the ring inner diameter and are rotated by $\pi/6$ obtained from (9). A total of $n_{pins} = 12$, obtained using (10) for $p = 1$ are integrated 1 mm from the edges of the inner diameter and rotated by $\pi/6$, computed using (11). Lastly, Ring D excites the quad-phase varying modes ($\vec{K}_{1,\pm4,4}$), with outer diameter $= 61.3$ mm. The ring is fed using P6 and P7 located 1.8 mm from the inner diameter $= 49.1$ mm, and rotated by $\alpha_3 = \pi/8$. It uses $n_{pins} = 16$ placed 1 mm from the inner diameter and rotated by $\alpha_{pins} = \pi/8$.

TABLE II
ANTENNA PERFORMANCE COMPARISONS BETWEEN FIG. 2 STRUCTURES FOR $\phi_a = 90°, \theta = 45°$ BEAM-STEERING DIRECTION.

l	Ant	Size ($\lambda \times \lambda \times \lambda$)	Isolation (dB)	Tot. Eff. (%)	10 dB IBW (MHz)	Directivity (dBi)	HPBW (°)	SLL (dB)
1	A	$0.27\lambda \times 0.27\lambda \times 0.038\lambda$	-	87	81	-1 (O)	-	-
3	A+B	$0.62\lambda \times 0.62\lambda \times 0.037\lambda$	31.2	73	34	3.95 (B)	88.7	-
5	A+B+C	$0.9\lambda \times 0.9\lambda \times 0.036\lambda$	23.2	55.8	32	7.08 (U)	95.4	-4.8
7	A+B+C+D	$1.18\lambda \times 1.18\lambda \times 0.036\lambda$	23	44.6	27	9.33 (U)	71.3	-7.3

l is the total number of excited modes, O-Omnidirectional, B-Bidirectional, and U-Unidirectional patterns.
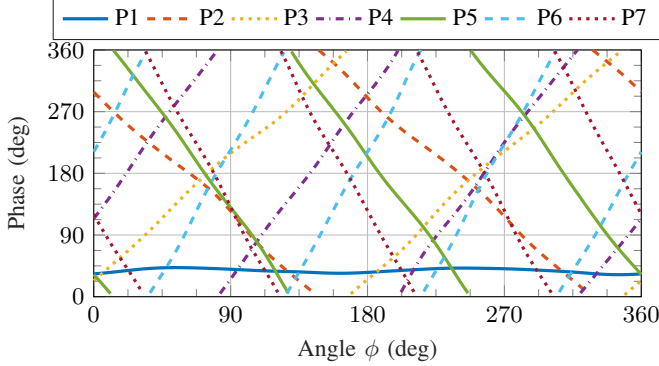

Fig. 5. Simulated phase of the radiation pattern for the final design (shown in Fig. 2) including structures A, B, C, and D.

TABLE I
FIG. 2 ANTENNA EXCITATION FOR $\phi_a = 90°, \theta = 45°$.

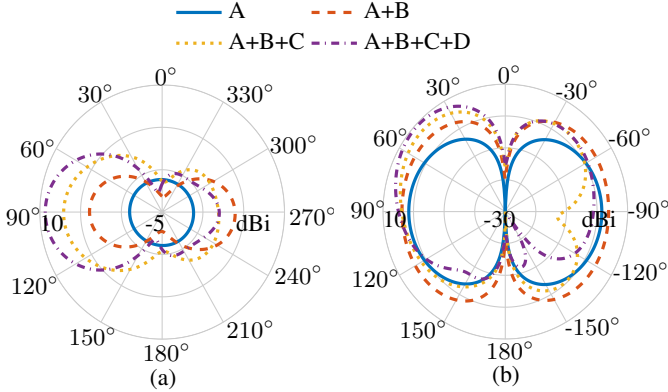| l	Ant.	$\Delta\beta_n(°)$						
		P1	P2	P3	P4	P5	P6	P7
1	A	0	-	-	-	-	-	-
3	A+B	0	189	275	-	-	-	-
5	A+B+C	0	277	198	278	16	-	-
7	A+B+C+D	0	275	191	14	270	186	269

Fig. 6. Proposed beam-steering performance of the design shown in Fig. 2 for $\phi_a = 90°, \theta = 45°$ direction: (a) $\theta = 45°$ cut; and (b) $\phi = 90°$ cut.

D. $360°$Azimuth plane Beam-Steering

Without loss of generality, we analyze the beam-steering capabilities by steering the beam towards $\phi_a = 90°$. All the ports exciting the phase-varying modes in the same ring are fed in quadrature. Fig. 5 shows the phase of the radiation pattern of the final design shown in Fig. 2, i.e. including all structures A, B, C, and D that generate respectively the fundamental mode $\vec{K}_{1,0,1}$, $\vec{K}_{1,\pm2,2}$ modes, the $\vec{K}_{1,\pm3,3}$ modes and the $\vec{K}_{1,\pm4,4}$.

The required $\Delta\beta_n$ to steer the main beam towards $\phi_a = 90°$ are shown in Table I and are computed using (8), i.e. no phase shift is added to P1 (exciting the $\vec{K}_{1,0,1}$ mode) and the phase shifts of the remaining ports is obtained by subtracting the phase value of P1 (at $\phi_a = 90°$ direction) with the respective port phase value (also at $\phi_a = 90°$ angle). The generated patterns are shown in Fig. 6, and the beam characteristics are outlined in Table II. It can be concluded that:

- A desired level of directivity can be realized by increasing the number of modes excited in the structure, e.g., for the configuration in Fig. 2, a directivity ≥ 7 dBi is achieved by exciting at least $l = 5$ modes (using A, B, and C).
- A and B combination provides the first type of beam-steering, a bidirectional one, where a second main beam is always located at $\phi_a + 180°$ (see Fig. 6).
- The smallest diameter to realize a unidirectional beam-steering is obtained using $n = 1, 2, 3$ modes (i.e., $l = 5$).
- Because higher-order modes have increased phase variations that require a much larger diameter, they present decreased bandwidth and total efficiency.
- Lastly, at the cost of a larger antenna diameter, an increase in the number of modes allows the generation of a much more selective beam pattern. This is seen from $l = 7$ modes, which present the lowest half-power beamwidth (HPBW), highest directivity, and lowest side-lobe level (SLL) compared to the other tested unidirectional pattern.

E. 3D Beam-Steering Antenna

To realize beam-steering across the azimuth and elevation planes, the first step is to select the type of beam-steering desired in the azimuth plane (e.g., bidirectional, unidirectional). Next, the number of modes required is selected according to the principle discussed in Section II-D. For the antenna proposed in this work, the lowest combination capable of beam-scanning in the azimuth plane is investigated, i.e., radiator A and B. It is understood that solely the omnidirectional modes of type $\vec{K}_{1,\pm n,n}$ cannot effectively control the beam outside the azimuth plane. Therefore, two orthogonal broad-side radiating modes are excited using an annular ring, i.e., the modes generating the main beam along the z-axis, with two modes corresponding to two orthogonal polarization. A single broadside mode will allow the structure to cover $\theta = 0°$ without any phase control. To steer the beam towards other θ directions, e.g., within xz- and yz-planes, the broadside modes are combined with the phase-varying $\vec{K}_{1,\pm n,n}$ modes.

Fig. 7a shows an antenna proposed for 3D beam-steering. The antenna is $h = 1.59$ mm thick, and uses the RO4003C
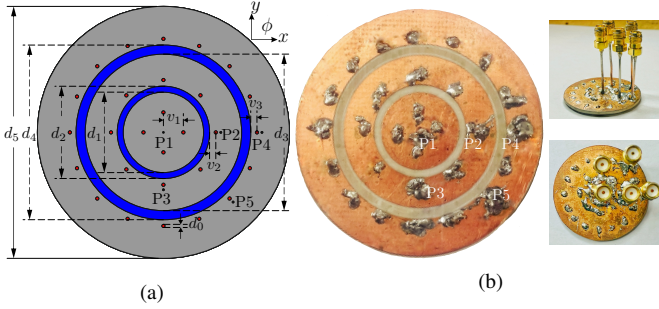
Fig. 7. Proposed antenna: (a) top view, dimensions (all in mm): $d_0 = 0.5, d_1 = 12.9, d_2 = 14.8, d_3 = 25.1, d_4 = 28, d_5 = 40.4, v_1 = 3.2, v_2 = v_3 = 1$; P2, P3, P4, and P5 feeding points are located 1.8 mm from the respective ring inner diameter; and (b) manufactured antenna, the left image shows the antenna top view, while the right images show the antenna bottom view to highlight the feeding system.
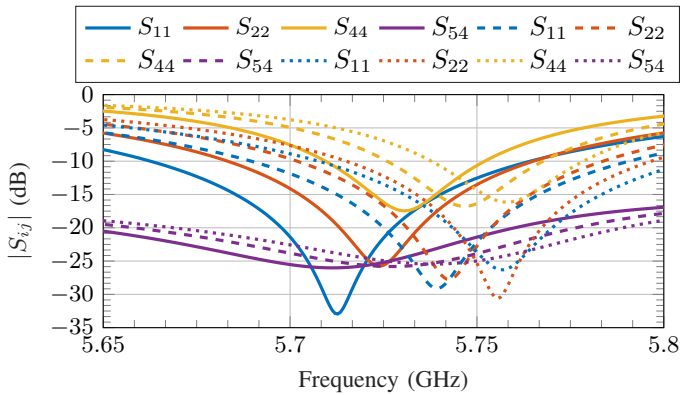

Fig. 8. Parametric results for different shorting pins diameter, with solid lines (for 0.49 mm diameter), dashed lines (for 0.5 mm diameter), and dotted lines (for 0.51 mm diameter). Note that due to symmetry between the modes excited on the same ring, only $|S_{22}|$ and $|S_{44}|$ are shown. Also, only the isolation of the ring exciting $n = 2$ modes ($|S_{45}|$) are shown for brevity.

Fig. 9. S-parameters results (solid lines: simulations, dashed lines: measurements), port index $i, j = 1, 2, 3, 4$, and, 5.

Fig. 10. Normalized radiation patterns of the antenna excited modes (solid lines: simulations, dashed lines: measurements): (a) omnidirectional spherical modes (xy-plane); and (b) broadside modes (xz-plane).

substrate. For azimuth scanning, the antenna excites $\vec{K}_{1,0,1}$ (using the center-fed circular patch), and $\vec{K}_{1,\pm2,2}$ modes (using the outer-most ring fed using P4 and P5); while two broadside modes are used to cover other planes, e.g. xz and yz-planes. These modes are excited using the first ring fed using P2 and P3 (rotated by $90°$) and include 8 shorting pins that are placed $v_2 = 1$ mm from the inner diameter and rotated by $45°$ with respect to the center. Please note that this function and the generated patterns differ from the ring B in Fig. 2.

The proposed antenna includes a total of 28 shorting pins, and all the pins have a diameter of 0.5 mm. During the prototype stage, the pins will consist of copper wires of 0.5 mm diameter, which typically have a tolerance of ±0.005 mm. To highlight the antenna robustness with respect to the shorting pins dimensions, we conducted parametric studies where the tolerance value was doubled to ±0.01 mm, i.e., the diameter was varied from 0.49 mm to 0.5 mm and 0.51 mm. The results are shown in Fig. 8. As expected, due to the inductance of the pins, the f_0 of each radiator shifts upwards as the diameter of the pins increases. However, it can also be noticed that only a slight frequency shift occurs, where f_0 is around 5.73, 5.75, and 5.76 GHz, for respectively 0.49, 0.5, and, 0.51 mm diameter. Additionally, the -10 dB impedance bandwidth changes
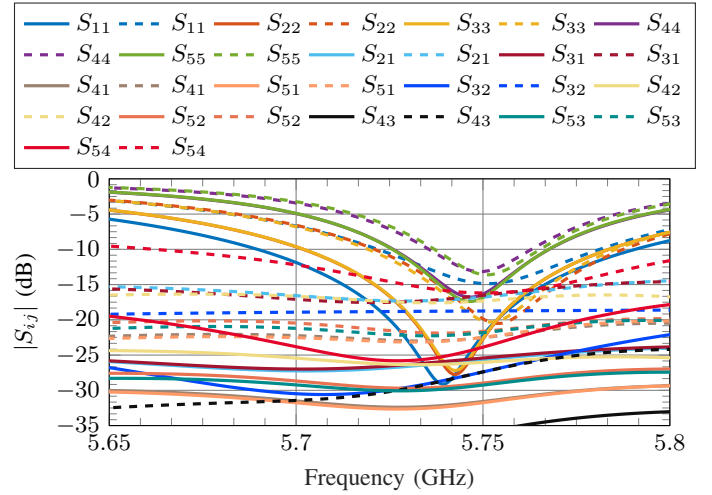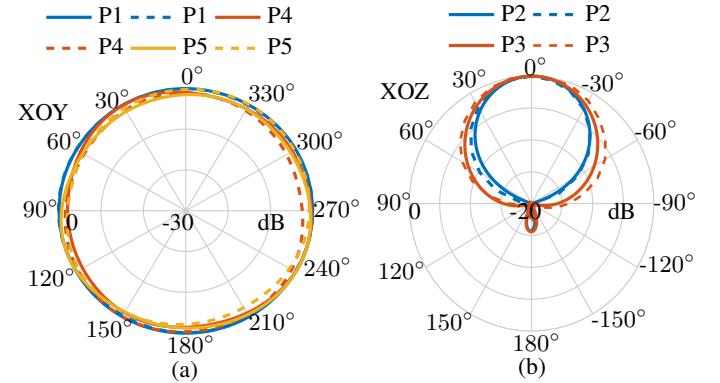
from 42.3, to 43, and, 41 MHz, when the diameter is increased from 0.49 to 0.51 mm, while the isolation stays around 24 dB in all the three cases. The results demonstrate that while slight frequency shifts may occur due to the tolerance of the pins, the isolation is little affected, and only slight changes in the impedance bandwidth are observed. The final diameter of the pins is therefore 0.5 mm, and the antenna final dimensions are 40.4 mm × 40.4 mm × 1.59 mm, or correspondingly $0.77\lambda \times 0.77\lambda \times 0.03\lambda$ for $f_0 = 5.75$ GHz.

III. FREE SPACE PERFORMANCE

Fig. 7b shows the image of the manufactured prototype. The antenna is probe fed using a $50\,\Omega$ semi-rigid coaxial cable, the Taoglas CAB.058 cable [36]. The connectors' inner conductor has a diameter of 0.287 mm, while the outer conductor has a diameter of 1.193 mm. The semi-rigid coaxial cable is used for antenna measurements. For integration within an on-body device (e.g., a smart watch), the antenna is intended to be placed on top of the device so that it can be directly probe-fed by its circuitry. The simulated and measured S-parameters are shown in Fig. 9. The f_0 in both cases is near 5.75 GHz. An isolation > 24 dB and a 42.2 MHz -10 dB Impedance
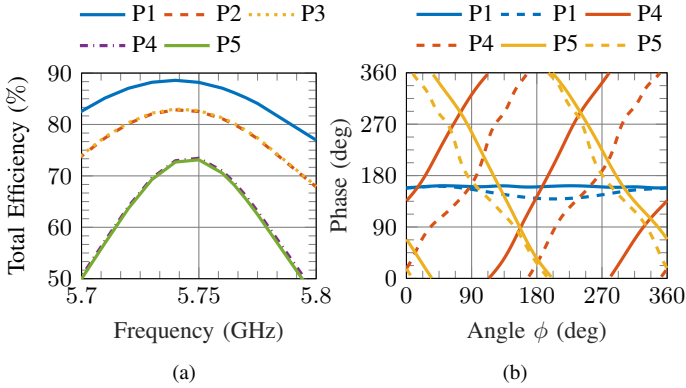
Fig. 11. Free space results: (a) simulated total efficiency for all ports; and (b) phase of the radiation pattern for the omnidirectional spherical modes, solid lines (simulations), and dashed lines (measurements).
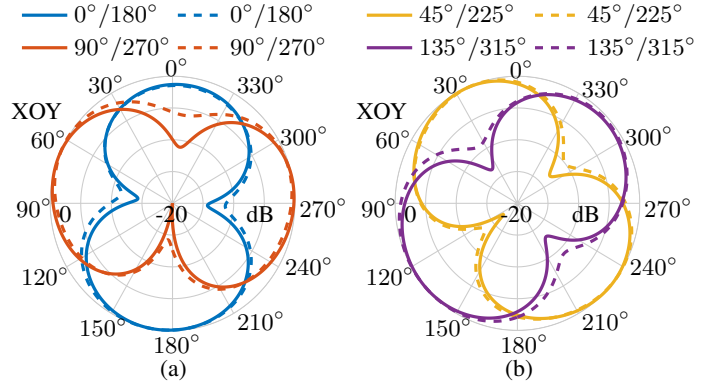

Fig. 12. Normalized radiation patterns showing the free space beam-steering in the azimuth plane, solid lines (simulations) and dashed lines (measurements): (a) $0°/180°$ and $90°/270°$; and (b) $45°/225°$ and $135°/315°$.

BandWidth (IBW) are obtained in simulations; decreasing to $16\,\mathrm{dB}$ and $31\,\mathrm{MHz}$ in measurements, respectively. Such discrepancies are most likely due to manufacturing tolerances.

Fig. 10 shows the simulated and measured radiation patterns, omnidirectional spherical modes (Fig. 10a), and broadside modes (Fig. 10b). Overall, a good agreement is demonstrated, and the required omnidirectional patterns are seen in Fig. 10a, while the broadside patterns have their main beam at $\theta = 0°$. Fig. 11a shows the simulated total efficiency for each port of the proposed antenna, where at f_0, the total efficiency is $88\%, 82.5\%, 82.7\%, 73\%$, and 73%, for P1, P2, P3, P4, and P5, respectively. The lowest efficiency and bandwidth limitations are observed for the dual-phase varying modes $\vec{K}_{1,\pm2,2}$ (excited using P4 and P5). These characteristics agree well with the performance highlighted in Section II-D, where a bidirectional beam-steering performance is realized as only the fundamental and the dual-phase varying modes are used.

The simulated peak realized gain at $5.75\,\mathrm{GHz}$ is $2.1\,\mathrm{dBi}$ (for P1), $8.58\,\mathrm{dBi}$ (P2), $8.61\,\mathrm{dBi}$ (P3), $4.25\,\mathrm{dBi}$ (P4), and $4.3\,\mathrm{dBi}$ (P5). The measured values change to $1.87\,\mathrm{dBi}$ (for P1), $7.21\,\mathrm{dBi}$ (P2), $7.15\,\mathrm{dBi}$ (P3), $3.51\,\mathrm{dBi}$ (P4), and $3.43\,\mathrm{dBi}$ (P5). It can be seen that the realized gain slightly deteriorates in the measured cases (especially for the ports exciting the dual-phase varying modes), where a discrepancy of up to $0.87\,\mathrm{dBi}$ is observed. Such variations are most likely due to substrate material tolerance and other manufacturing inaccuracies.

Lastly, the Envelope Correlation Coefficient (ECC) is calculated from the complex 3D radiation patterns using [37]

$$\rho_{ECC} = \frac{\iint_{4\pi} \vec{E}_i \cdot \vec{E}_j^* d\Omega}{\sqrt{\iint_{4\pi} \vec{E}_i \cdot \vec{E}_i^* d\Omega \iint_{4\pi} \vec{E}_j \cdot \vec{E}_j^* d\Omega}} \quad (12)$$

where $\vec{E}_i$ and $\vec{E}_j$ are the far-field radiation patterns from ports $i, j = 1, 2, 3, 4,$ and, 5. The ECC stays below 0.001 within the entire bandwidth and is $\leq 3 \times 10^{-4}$ at $f_0 = 5.75\,\mathrm{GHz}$.

A. Free Space Azimuth Plane Beam-Steering

The phase characteristics of the excited omnidirectional modes are shown in Fig. 11b for the simulated and measured cases in the azimuth plane. In both scenarios, the patterns have

TABLE III
EXCITATIONS FOR AZIMUTH PLANE BEAM-STEERING

Beam direction	$\Delta\beta_1$	$\Delta\beta_4$	$\Delta\beta_5$
$\phi = 0°/180°$	$0°\ (0°)$	$135°\ (218°)$	$135°\ (218°)$
$\phi = 45°/225°$	$0°\ (0°)$	$45°\ (125°)$	$243°\ (302°)$
$\phi = 90°/270°$	$0°\ (0°)$	$359°\ (45°)$	$358°\ (43°)$
$\phi = 135°/335°$	$0°\ (0°)$	$219°\ (291°)$	$39°\ (113°)$

The three ports are fed with similar magnitude $|A_i| = 1$, and the values inside parentheses are for on-body measured cases.

the desired dual-phase variations, where the phase changes in two opposing directions as required for the $\vec{K}_{1,\pm2,2}$ modes (please see P4 and P5), while P1 has a constant phase (as it excites the $\vec{K}_{1,0,1}$ mode). The small discrepancies seen in the measured case may be due to the manufacturing tolerances.

To test the antenna beam-steering capabilities, the main beam was steered towards four different directions separated by $90°$ to cover the entire plane. Fig. 12 shows the beam-steering performance, where Fig. 12a depicts the beam-steering for $0°/180°$ and $90°/270°$ directions. Fig. 12b highlights the beam-steering for $45°/225°$ and $135°/315°$ directions. The required phase shifts to steer the beams toward the desired directions are computed based on the phase values shown in Fig. 11b and using (8). The calculated phase shifts for the measured beam-steering results are detailed in Table III. A good agreement is realized between the two cases, with the generated main beams covering the desired directions. The few discrepancies seen in the measured cases (beamwidth, shouldering, and dips) may be due to the small phase dips in measurements and other manufacturing tolerances.

B. Free Space Elevation Plane Beam-Steering

Fig. 13a shows the xz-plane beam-steering ($\phi = 0°$), while the $yz-$plane ($\phi = 90°$) beam-steering is given in Fig. 13b. This performance is obtained by exciting one phase-varying omnidirectional spherical mode (P4 or P5) and one broadside radiating mode (P2 or P3). For completeness, Table IV outlines the excitation used to generate the elevation plane beam-steering. It can be seen that a slight discrepancy (of up to $2°$) occurs in the direction of the steered beams between
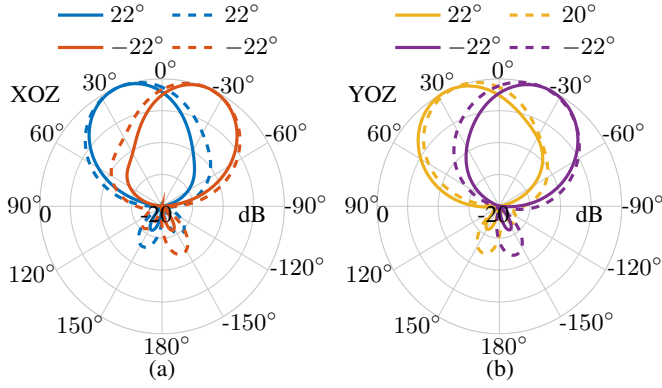
Fig. 13. Normalized radiation patterns of the elevation plane beam-steering, solid lines (simulations), and dashed lines (measurements): (a) xz-plane results; and (b) $yz-$plane results.

TABLE IV
EXCITATIONS FOR ELEVATION PLANE BEAM-STEERING

Beam direction	$|A_2|$	$\Delta\beta_2$	$|A_4|$	$\Delta\beta_4$	$|A_5|$	$\Delta\beta_5$
$\phi=0°, \theta=22°$	1	0°	-	-	1	0°
$\phi=0°, \theta=-22°$	1	0°	-	-	1	180°
$\phi=90°, \theta=20°$	1	0°	1	0°	-	-
$\phi=90°, \theta=-22°$	1	0°	1	180°	-	-

the simulated and measured results in the yz-plane. Note that the beam-steering direction can be further optimized by controlling the magnitude and phase shifts of the antenna ports. However, for brevity, only similar excitation configurations (in simulations and measurements) are demonstrated. Overall, a good agreement is realized, with the slight increase in beamwidth of the measured cases being attributed to the discrepancies highlighted in the measured broadside modes and the phase characteristics of the omnidirectional modes (P4 and P5). Note that when the main beam is steered towards a given θ direction (e.g., $+\theta$), a phase inversion of $180°$, changes the main beam direction, i.e., the main beam will be located at $-\theta$. Also, note that different combinations between the broadside and dual-phase varying spherical modes can be used to cover the elevation plane; however, for brevity, only the combination of P2, P4, and P5 without amplitude control is used in the patterns shown in Fig. 13.

IV. ON-BODY PERFORMANCE

To investigate the antenna performance for on-body applications, a multi-layer phantom is used (see Fig. 14). In the simulation, the phantom comprises three layers: skin layer (thickness of $1.3\,\text{mm}$), fat layer ($10.5\,\text{mm}$ thick), and muscle layer ($20\,\text{mm}$ thick), where the dimensions are approximated from [25]. The antenna is first placed in direct contact with the multi-layer phantom, i.e., the gap between the antenna ground plane and the phantom is $0\,\text{mm}$. For measurements, a pork trunk of size $110\,\text{mm} \times 70\,\text{mm} \times 31\,\text{mm}$ is used, and the measurement setup is shown in Fig. 16a.

Fig. 15 shows the S-parameters results for the on-body setup. For both cases, simulations, and measurements, it is seen that the center frequency ($f_0 = 5.75\,\text{GHz}$) shifts to
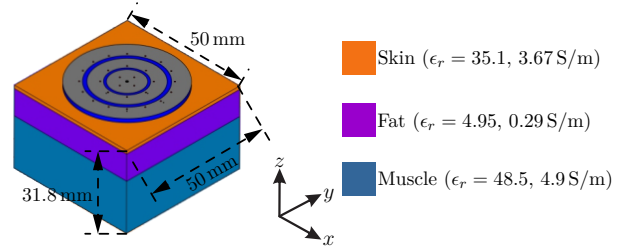

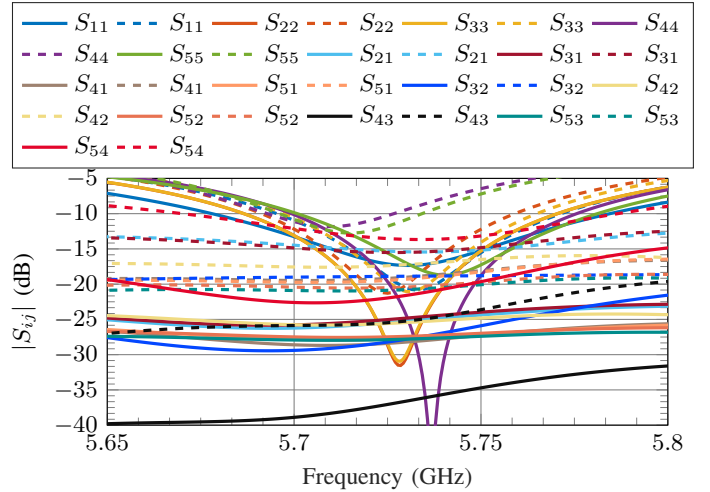Fig. 14. Proposed on-body setup using a three-layer phantom.

Fig. 15. On-body S-parameters results (solid lines: simulations, dashed lines: measurements), port index $i, j = 1, 2, 3, 4$, and, 5.

TABLE V
TOTAL EFFICIENCY FOR DIFFERENT GAP VALUES

gap	Total Efficiency				
	P1	P2	P3	P4	P5
0 mm	82%	81%	80%	58.7%	61%
1 mm	83.5%	81.4%	80.5%	61%	63%
2 mm	84%	81.5%	80.8%	63%	65%
3 mm	85%	81.8%	81%	64.5%	66%
free space	88%	82.5%	82.7%	73%	73%

lower values compared to the free space case, i.e., $5.73\,\text{GHz}$ (on-body simulated), and $5.71\,\text{GHz}$ (on-body measured). Due to the phantom, in simulations, the isolation deteriorates to $21\,\text{dB}$, and IBW changes to $67\,\text{MHz}$ (compared to $24\,\text{dB}$ and $42.2\,\text{MHz}$ in free space). For the measured case the isolation and IBW change from $16\,\text{dB}$ and $31\,\text{MHz}$ in free space to $13.2\,\text{dB}$ and $29\,\text{MHz}$ with the phantom. Table V shows the total efficiency of each antenna port when the gap between the antenna ground plane and the phantom is increased from 0 to $3\,\text{mm}$, along with the free space case values. It can be seen that the total efficiency increases as the gap increases, and the best values are seen for the free space scenario. Additionally, these results show that the most significant efficiency drop due to the phantom occurs for ports P4 and P5. This may be explained by the dual-phase change of the modes excited by these ports ($\vec{K}_{1,\pm2,2}$ modes), which require a much larger diameter to support these variations. In contrast, the highest efficiency is seen for the fundamental mode ($K_{1,0,1}$ mode excited using
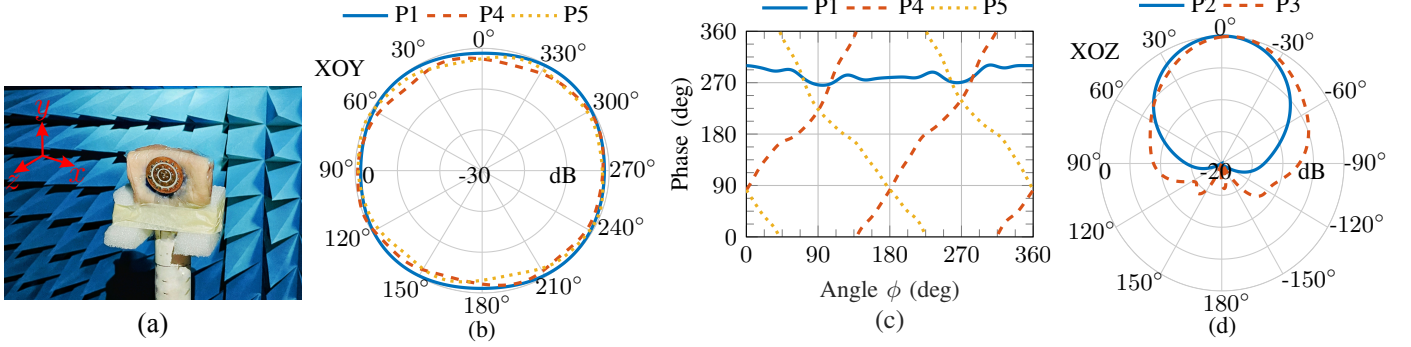
Fig. 16. On-body measured performance: (a) measurement setup; (b) normalized measured radiation patterns of the excited omnidirectional spherical modes; (c) measured phase characteristics of the respective omnidirectional spherical modes; and (d) normalized measured radiation patterns of the broadside modes.
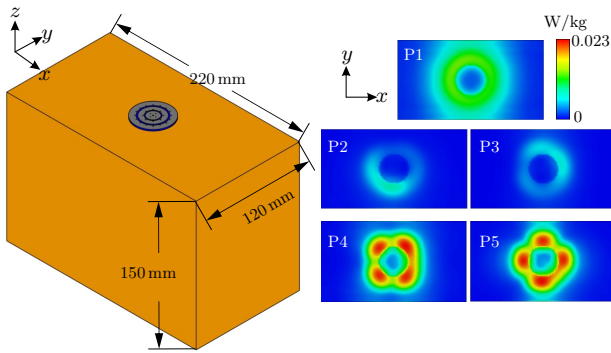

Fig. 17. SAR analysis following FCC guidelines for the wrist-worn setup.

P1), which has a constant phase across the azimuth plane. Nevertheless, the total efficiency of the ports exciting the dual-phase varying modes is still above 58% for the worst investigated case, i.e., with gap $= 0\,\text{mm}$.

A. Specific Absorption Rate (SAR)

To investigate the electromagnetic (EM) field exposure, the SAR is computed following the FCC guidelines [38]. The setup is shown in Fig. 17, and for the wrist-worn condition, the antenna is placed in direct contact with a block filled with human hand tissue ($\epsilon_r = 21.3$, $\delta = 0.51\,\text{S/m}$, and $\rho = 1000\,\text{kg/m}^3$), averaged $10\,\text{g}$, with an input power of $10\,\text{mW}$. As shown in Fig. 17, the peak SAR values for each port are $0.0073\,\text{W/kg}$ (for P1), $0.0024\,\text{W/kg}$ (P2), $0.0032\,\text{W/kg}$ (P3), $0.023\,\text{W/kg}$ (P4 and P5). Therefore, the antenna peak SAR value is $0.023\,\text{W/kg}$, which is well below the $4\,\text{W/kg}$ (FCC) [38] and (ICNIRP) [39] SAR limits.

The results also show that the omnidirectional modes (P1, P4, and P5) have the highest SAR values for this setup compared to the broadside radiating modes. This can be explained by the fact that when the antenna is mounted on the phantom, the omnidirectional modes have strong $\vec{E}$-fields along the phantom length and its depth ($-z$ direction), which results in more EM absorption by the human tissue. In contrast, for P2 and P3, since their main beam is pointing towards $+z$ (away from the phantoms' depth and length), the EM absorption by the tissue is consequently smaller.

B. On-Body Beam-Steering

The on-body measurement setup is shown in Fig. 16a. The measured patterns of the omnidirectional modes are shown in Fig. 16b, and the respective phase properties are shown in Fig. 16c. The measured broadside patterns are shown in Fig. 16d. Due to the phantom, the radiation patterns of the omnidirectional spherical modes exhibit shouldering and dips, especially for P4 and P5. This can also be explained by the SAR analysis, where higher SAR values are seen for the omnidirectional modes. In general, the required phase properties are still satisfied. It should also be mentioned that the reflections from the antenna holder and other materials used for the on-body measurement may also explain the above-described pattern dips, shoulders, and phase asymmetries. Lastly, the main beam in the broadside radiating modes (P2 and P3) is not significantly affected, as it radiates towards $+z$. However, some impact on the patterns is seen around the ($-z$) direction, especially for the P3 excited mode. This is because P3 is an x-polarized mode, and the length of the pork trunk is larger along the x-direction than the y-direction. The simulated peak realized gain for the on-body scenario at f_0 is $1.4\,\text{dBi}$ (for P1), $7.76\,\text{dBi}$ (P2), $7.8\,\text{dBi}$ (P3), $2.78\,\text{dBi}$ (P4), and $2.91\,\text{dBi}$ (P5). These values decrease to $0.81\,\text{dBi}$ (for P1), $6.41\,\text{dBi}$ (P2), $6.32\,\text{dBi}$ (P3), $1.53\,\text{dBi}$ (P4), and $1.6\,\text{dBi}$ (P5) for the measured setup. It can be seen that a $1.3\,\text{dBi}$ realized gain deterioration occurs between the simulated and measured cases. This is most likely due to the manufacturing tolerances and the differences in dielectric properties between the phantom used in simulations and the actual pork trunk that was used for on-body measurements.

Fig. 18 shows the azimuth plane on-body beam-steering for both the simulated and measured cases. The main beam is steered in four directions, separated by $90°$ to cover the entire plane, with Fig. 18a showing the beam-steering performance for $0°/180°$ and $90°/270°$ directions. In comparison, Fig. 18b highlights the performance for $45°/225°$ and $135°/315°$ directions. It can be seen that in both cases, simulated and measured, the antenna can direct the beam in all the desired directions, demonstrating good beam-steering characteristics. The small dips in the measured $0°/180°$ pattern and the beamwidth discrepancies are due to asymmetries of the pork

TABLE VI
COMPARISONS WITH PREVIOUSLY PUBLISHED ON-BODY ANTENNAS

Ref.	Freq. (GHz)	Size ($\lambda \times \lambda$)	Profile (λ)	Peak Gain (dBi)	Structure	Elev. Steer	Range	Azim. Steer	Range
[18]	6.0	1.2×0.6	0.03	6.69	Planar	Yes	$yz \, (-31°, 0°, 30°)$	No	NA
[23]	2.35/5.8	$0.54 \times 0.54*$	0.012	5.4	Planar	B#	NA	O#	NA
[19]	2.4	0.8×0.8	0.027	3.9	Planar	B#	NA	O#	NA
[6]	2.45/5.8	0.18×0.18	0.04	2.74	Non-planar	B#	NA	O#	NA
[20]	2.45	0.55×0.55	0.051	7.15 sim.	Stacked	B#	NA	O#	NA
[21]	2.45	0.39×0.39	0.026	3.83	Planar	B#	NA	O#	NA
[22]	2.44	0.34×0.34	0.056	2	Non-planar	BD,O	NA	No	NA
[28]	2.45	0.83×0.83	0.012	6	Planar	B#	NA	O#	NA
[29]	2.4	0.45×0.45	0.021	3.86	Planar	B#	NA	O#	NA
Prop.	5.71	0.77×0.77	0.03	6.41	Planar	Yes	$xz(32°)$, $yz(33°)$	Yes	$360°$

*(Excluding ground plane size), # dual-pattern synthesis (O-Omnidirectional, B-Broadside, BD-Bidirectional), NA (Not applicable).
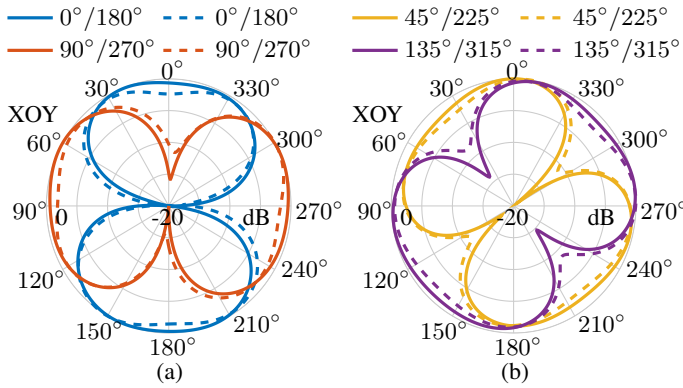

Fig. 18. Normalized radiation patterns showing the on-body beam-steering in the azimuth plane, solid lines (simulations) and dashed lines (measurements): (a) $0°/180°$ and $90°/270°$; and (b) $45°/225°$ and $135°/315°$.
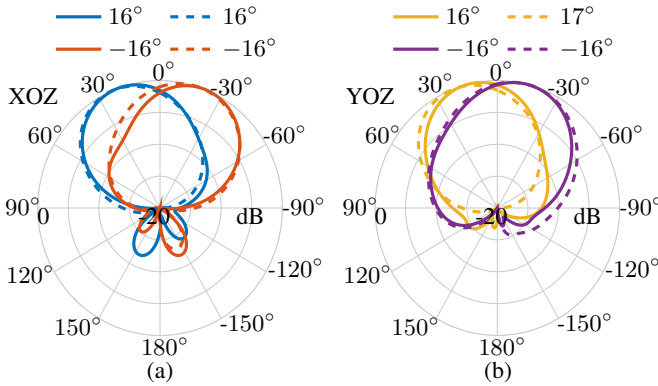

Fig. 19. Normalized radiation pattern results for the elevation plane on-body beam-steering, solid lines (simulations), and dashed lines (measurements): (a) xz-plane; and (b) $yz-$plane.

phantom, manufacturing tolerances, and the effects of the antenna holder. For completeness, the excitations for each beam direction are shown in Table III.

The simulated and measured results for the elevation plane beam-steering are shown in Fig. 19, where the xz-plane beam-steering performance is shown in Fig. 19a, while the yz-plane results are shown in Fig. 19b, both are obtained using similar excitations as those outlined in Table IV. It can be seen that good beam-steering characteristics are realized in both planes. A slight increase in the beamwidth is seen for the measured cases, and a $1°$ discrepancy in the main beam direction is observed in the yz-plane. Such discrepancies may be the result of the combined effects of the phantom, antenna holder, and other manufacturing inaccuracies. The scanning range in the elevation plane for the on-body setup is lower compared to the free space case, changing from $44°$ to $32°$ (for the xz-plane) and from $44°$ to $33°$ (for the yz-plane). It is interesting to point out that this range can be further enhanced with our proposed beam-steering solution, mainly by adding a ring to excite the omnidirectional spherical modes with higher phase variations.

Finally, Table VI compares the proposed antenna with previously published on-body antennas. It is seen that, unlike previous works, the design is capable of continuous beam-steering over the entire azimuthal plane with good scanning in the elevation plane. Therefore, it represents a significant breakthrough to enable advanced wireless applications in on-body IoT devices.

V. CONCLUSION

A compact antenna ($0.77\lambda \times 0.77\lambda \times 0.03\lambda$) is proposed for 3D beam-steering in on-body IoT applications. By exploiting the theory of spherical modes, advanced beam-steering is demonstrated in the xy-plane while using planar structures. The method is shown to support beam-steering in the xz and yz-planes by exciting two orthogonal broadside modes. For on-body scenarios, the antenna has a $360°$ scanning range in the xy-plane, while a scanning range of $32°$ and $33°$ is realized in the xz and yz-planes, respectively. This performance is achieved with a total efficiency $> 58\%$, and measured peak realized gain of up to $6.41\,\mathrm{dBi}$. The antenna is manufactured using a single printed layer. The 3D beam-steering characteristics are achieved without externally controlled switches, supporting the generation of multiple simultaneous patterns at the same frequency, i.e. digital beamforming. Overall, the design is compact, low-profile, planar, suitable for packaging with emerging on-body IoT devices, and compatible with many advanced wireless applications like MIMO, angle of arrival-based localization, and physical layer security.

REFERENCES

[1] Y. Zhou *et al.*, "Design and Evaluation of Pattern Reconfigurable Antennas for MIMO Applications," *IEEE Trans. Antennas. Propag.*, vol. 62, no. 3, pp. 1084–1092, 2014.

[2] H. Li, B. K. Lau, and S. He, "Design of Closely Packed Pattern Reconfigurable Antenna Array for MIMO Terminals," *IEEE Trans. Antennas. Propag.*, vol. 65, no. 9, pp. 4891–4896, 2017.

[3] Q. Luo *et al.*, *Low-Cost Beam-Reconfigurable Directional Antennas for Advanced Communications*. John Wiley & Sons, Ltd, 2022, ch. 3, pp. 83–117.

[4] D. Rodrigo, L. Jofre, and B. A. Cetiner, "Circular Beam-Steering Reconfigurable Antenna With Liquid Metal Parasitics," *IEEE Trans. Antennas. Propag.*, vol. 60, no. 4, pp. 1796–1802, 2012.

[5] P.-Y. Qin, Y. J. Guo, and C. Ding, "A Beam Switching Quasi-Yagi Dipole Antenna," *IEEE Trans. Antennas. Propag.*, vol. 61, no. 10, pp. 4891–4899, 2013.

[6] L. Zhang *et al.*, "Planar Ultrathin Small Beam-Switching Antenna," *IEEE Trans. Antennas. Propag.*, vol. 64, no. 12, pp. 5054–5063, 2016.

[7] M.-C. Tang, B. Zhou, and R. W. Ziolkowski, "Low-Profile, Electrically Small, Huygens Source Antenna With Pattern-Reconfigurability That Covers the Entire Azimuthal Plane," *IEEE Trans. Antennas. Propag.*, vol. 65, no. 3, pp. 1063–1072, 2017.

[8] J. Ouyang *et al.*, "Center-Fed Unilateral and Pattern Reconfigurable Planar Antennas With Slotted Ground Plane," *IEEE Trans. Antennas. Propag.*, vol. 66, no. 10, pp. 5139–5149, 2018.

[9] T. Liang, Y. Pan, and Y. Dong, "Miniaturized Pattern Reconfigurable Multi-Mode Antennas with Continuous Beam Steering Capability," *IEEE Trans. Antennas. Propag.*, pp. 1–1, 2023.

[10] T. Q. Tran and S. K. Sharma, "Radiation Characteristics of a Multimode Concentric Circular Microstrip Patch Antenna by Controlling Amplitude and Phase of Modes," *IEEE Trans. Antennas. Propag.*, vol. 60, no. 3, pp. 1601–1605, 2012.

[11] M. Li *et al.*, "Compact Surface-Wave Assisted Beam-Steerable Antenna Based on HIS," *IEEE Trans. Antennas. Propag.*, vol. 62, no. 7, pp. 3511–3519, 2014.

[12] W. Lin, H. Wong, and R. W. Ziolkowski, "Wideband Pattern-Reconfigurable Antenna With Switchable Broadside and Conical Beams," *IEEE Antennas Wireless Propag. Lett.*, vol. 16, pp. 2638–2641, 2017.

[13] M. A. Towfiq *et al.*, "A Reconfigurable Antenna With Beam Steering and Beamwidth Variability for Wireless Communications," *IEEE Trans. Antennas. Propag.*, vol. 66, no. 10, pp. 5052–5063, 2018.

[14] A. H. Naqvi and S. Lim, "A Beam-Steering Antenna With a Fluidically Programmable Metasurface," *IEEE Trans. Antennas. Propag.*, vol. 67, no. 6, pp. 3704–3711, 2019.

[15] A. Zandamela, N. Marchetti, and A. Narbudowicz, "Stacked-Patch MIMO Antenna for Dual-Plane Beamsteering," in *2021 IEEE International Symposium Antennas Propag. USNC-URSI Radio Science Meeting (APS/URSI)*, 2021, pp. 311–312.

[16] ——, "Compact Stacked-Patch Antenna for Directional Modulation in Azimuth and Elevation Planes," in *2022 IEEE International Symposium Antennas Propag. USNC-URSI Radio Science Meeting (AP-S/URSI)*, 2022, pp. 1206–1207.

[17] Y. Zhang *et al.*, "A Highly Pattern-Reconfigurable Planar Antenna With 360° Single- and Multi-Beam Steering," *IEEE Trans. Antennas. Propag.*, vol. 70, no. 8, pp. 6490–6504, 2022.

[18] S.-J. Ha and C. W. Jung, "Reconfigurable Beam Steering Using a Microstrip Patch Antenna With a U-Slot for Wearable Fabric Applications," *IEEE Antennas Wireless Propag. Lett.*, vol. 10, pp. 1228–1231, 2011.

[19] S. Yan and G. A. E. Vandenbosch, "Radiation Pattern-Reconfigurable Wearable Antenna Based on Metamaterial Structure," *IEEE Antennas Wireless Propag. Lett.*, vol. 15, pp. 1715–1718, 2016.

[20] R. Masood, C. Person, and R. Sauleau, "A Dual-Mode, Dual-Port Pattern Diversity Antenna for 2.45-GHz WBAN," *IEEE Antennas Wireless Propag. Lett.*, vol. 16, pp. 1064–1067, 2017.

[21] X. Tong *et al.*, "Switchable ON-/OFF-Body Antenna for 2.45 GHz WBAN Applications," *IEEE Trans. Antennas. Propag.*, vol. 66, no. 2, pp. 967–971, 2018.

[22] D. Wen *et al.*, "Design of a MIMO Antenna With High Isolation for Smartwatch Applications Using the Theory of Characteristic Modes," *IEEE Trans. Antennas. Propag.*, vol. 67, no. 3, pp. 1437–1447, 2019.

[23] Z. G. Liu and Y. X. Guo, "Dual Band Low Profile Antenna for Body Centric Communications," *IEEE Trans. Antennas. Propag.*, vol. 61, no. 4, pp. 2282–2285, 2013.

[24] S.-W. Su and Y.-T. Hsieh, "Integrated Metal-Frame Antenna for Smartwatch Wearable Device," *IEEE Trans. Antennas. Propag.*, vol. 63, no. 7, pp. 3301–3305, 2015.

[25] X.-Q. Zhu, Y.-X. Guo, and W. Wu, "Miniaturized Dual-Band and Dual-Polarized Antenna for MBAN Applications," *IEEE Trans. Antennas. Propag.*, vol. 64, no. 7, pp. 2805–2814, 2016.

[26] D. Wu and S. W. Cheung, "A Cavity-Backed Annular Slot Antenna With High Efficiency for Smartwatches With Metallic Housing," *IEEE Trans. Antennas. Propag.*, vol. 65, no. 7, pp. 3756–3761, 2017.

[27] B. Wang and S. Yan, "Design of smartwatch integrated antenna with polarization diversity," *IEEE Access*, vol. 8, pp. 123 440–123 448, 2020.

[28] H. Sun *et al.*, "Design of Pattern-Reconfigurable Wearable Antennas for Body-Centric Communications," *IEEE Antennas Wireless Propag. Lett.*, vol. 19, no. 8, pp. 1385–1389, 2020.

[29] G.-P. Gao *et al.*, "A Compact Dual-Mode Pattern-Reconfigurable Wearable Antenna for the 2.4-GHz WBAN Application," *IEEE Trans. Antennas. Propag.*, vol. 71, no. 2, pp. 1901–1906, 2023.

[30] A. Zandamela *et al.*, "Spherical Modes Driven Directional Modulation With a Compact MIMO Antenna," *IEEE Antennas Wireless Propag. Lett.*, vol. 22, no. 3, pp. 477–481, 2023.

[31] W. W. Hansen, "A New Type of Expansion in Radiation Problems," *Phys. Rev.*, vol. 47, pp. 139–143, Jan 1935. [Online]. Available: https://link.aps.org/doi/10.1103/PhysRev.47.139

[32] J. E. Hansen, Ed., *Spherical Near-field Antenna Measurements*, ser. Electromagnetic Waves. IET, 1988.

[33] F. Jensen, "Electromagnetic Near-field - Far-field Correlations," PhD thesis, Technical University of Denmark, Laboratory of Electromagnetic Theory, July 1970.

[34] "Microstrip antenna design handbook," R. Garg, P. Bhartia, B. I., and A. Ittipboon, Eds. Norwood, MA: Artech House, 2001, ch. 5.

[35] J. Liu, Q. Xue, H. Wong, H. W. Lai, and Y. Long, "Design and analysis of a low-profile and broadband microstrip monopolar patch antenna," *IEEE Trans. Antennas. Propag.*, vol. 61, no. 1, pp. 11–18, 2013.

[36] TAOGLAS. CAB.058 SMA(F)Jack to 3/3mm 0.047" Strip/Tin Semi-Rigid Cable 50mm(including Connectors). Accessed: 2023-11-01. [Online]. Available: https://www.taoglas.com/product/cab058-smafjack-to-33mm-0-047-striptin-semi-rigid-cable-50mmincluding-connectors/

[37] M. S. harawi, "Current Misuses and Future Prospects for Printed Multiple-Input, Multiple-Output Antenna Systems [Wireless Corner]," *IEEE Antennas Propag. Mag.*, vol. 59, no. 2, pp. 162–170, 2017.

[38] R. E. Fields, *Evaluating compliance with FCC guidelines for human exposure to radiofrequency electromagnetic fields*. Federal Communications Commission Office of Engineering & Technology, 1997. [Online]. Available: https://transition.fcc.gov/bureaus/oet/info/documents/bulletins/oet65/oet65a.pdf

[39] International Commission on Non-Ionizing Radiation Protection (IC-NIRP), "Guidelines for Limiting Exposure to Electromagnetic Fields (100 kHz to 300 GHz)," *Health Physics*, vol. 118, no. 5, pp. 483–524, 2020.

Abel Zandamela (Graduate Student Member, IEEE) received his B.Eng. in Information Engineering from South China University of Technology in 2017, his M.Eng. in Electrical and Software Systems Engineering from King Mongkuts University of Technology North Bangkok, Thailand, in 2019. From 2018 to 2020, he was with the Institute of High Frequency Technology (IHF) of RWTH Aachen University, Germany. He is currently a Ph.D. candidate at Trinity College Dublin, Ireland. His research interests include electrically small antennas, beamsteering antennas, wireless physical layer security, on-body antennas, MIMO antennas, IoT localization systems, and leaky-wave antennas. He received the IEEE 2022 AP-S Doctoral Research Grant, the Prof. Tom Brazil CONNECT Research Center Excellence in Research 2022 Student Award, the TICRA–EurAAP grant for the 2022 EuCAP, and the IEEE 2021 AP-S C.J. Reddy travel grant.

Nicola Marchetti (Senior Member, IEEE) is Associate Professor in Wireless Communications at Trinity College Dublin, Republic of Ireland, where he leads the Wireless Engineering and Complexity Science lab (WhyCOM). He is an IEEE Communications Society Distinguished Lecturer, and a Fellow of Trinity College Dublin. He received the PhD in Wireless Communications from Aalborg University, Denmark in 2007, the MSc in Electronic Engineering from University of Ferrara, Italy in 2003, and the MSc in Mathematics from Aalborg University in 2010. He has authored more than 180 journals and conference papers, 2 books and 9 book chapters, holds 4 patents, and received 4 best paper awards. His research interests span AI for Future Networks, Bio-Inspired and Bio-Enabled Networks, Complex and Self-Organising Networks, MAC Protocols and Radio Resource Management, Signal Processing for Communications, and Quantum Communications and Networks. He has served as an Associate Editor for the IEEE Internet of Things Journal and the EURASIP Journal on Wireless Communications and Networking.

Max J. Ammann (Fellow, IEEE) received the Ph.D. degree in antennas and propagation from Trinity College Dublin, University of Dublin, Ireland, in 1997. He is a Professor of antennas and propagation at the School of Electrical and Electronic Engineering, Technological University Dublins, Dublin, and the Director of the Antennas and High-Frequency Research Centre. He became a Chartered Engineer in 1986. He has more than 200 peer-reviewed articles published in journals and international conferences. His research interests include electromagnetic theory, antenna miniaturization for terminal and ultrawideband applications, antennas for medical devices, and antenna issues relating to privacy.

Dr. Ammann is a member of the IEEE International Committee for Electromagnetic Safety. His team received 13 Best Paper Awards at International Conferences on Antennas and Propagation and seven Commercialization Awards. He has served as an Expert in the industry on various antenna technologies in communications, medical, aviation, and electronic security sectors in Ireland and Abroad. He acted as an Associate Editor for the IEEE Antennas and Wireless Propagation Letters from 2012 to 2018. He has Co-Chaired IWAT2022 in Dublin and various workshops on antennas and related technologies.

Adam Narbudowicz Adam Narbudowicz (Senior Member, IEEE) received M.Sc. from Gdansk University of Technology, Poland, in 2008, Ph.D. from the Dublin Institute of Technology (now TU Dublin), Ireland, in 2013, and Habilitation from Wroclaw University of Science and Technology, Poland, in 2020. He is currently an senior researcher at Trinity College Dublin and a part-time associate professor at Wroclaw University of Science and Technology. He was twice a postdoctoral fellow of Marie Sklodowska-Curie Action co-funded projects, including a two-year research stay at RWTH Aachen University, Germany. His research interests include antenna miniaturization and reconfigurable antenna, sustainable antenna technology, and the use of machine learning for radar applications.

Dr. Narbudowicz has co-authored more than 80 scientific publications in journals and peer-reviewed conference proceedings. He was selected as 2023 IEEE APS Young Professional Ambassador, received the Scholarship for Outstanding Young Polish Scientists in 2019, the Inaugural 2018 Prof. Tom Brazil CONNECT Excellence in Research Award, the best poster by popular vote at the 2018 IEEE-EURASIP Summer School on Signal Processing, the 3rd Best Paper Award during ISAP 2017, and the DIT Inventor Competition Award for Best Postgraduate/Staff Invention in 2012. He was also a mentor to the finalist team of the 2020 IEEE AP-S Student Design Contest. He sits on the Management Committee of the COST action SyMat, and serves as the Vice-Chair for EurAAP Small Antenna Working Group and IEEE Poland APS/MTT/AES Joint Chapter.